The Astrophysical Journal, 716:746–757, 2010 June 10 doi:10.1088/0004-637X/716/1/746

AMiBA WIDEBAND ANALOG CORRELATOR

Chao-Te Li[1], Derek Y. Kubo[1], Warwick Wilson[2], Kai-Yang Lin[1,3], Ming-Tang Chen[1], P. T. P. Ho[1,4], Chung-Cheng Chen[1], Chih-Chiang Han[1], Peter Oshiro[1], Pierre Martin-Cocher[1], Chia-Hao Chang[1], Shu-Hao Chang[1], Pablo Altamirano[1], Homin Jiang[1], Tzi-Dar Chiueh[3], Chun-Hsien Lien[3], Huei Wang[3], Ray-Ming Wei[3], Chia-Hsiang Yang[3], Jeffrey B. Peterson[5], Su-Wei Chang[1], Yau-De Huang[1], Yuh-Jing Hwang[1], Michael Kesteven[2], Patrick Koch[1], Guo-Chin Liu[1,6], Hiroaki Nishioka[1], Keiichi Umetsu[1], Tashun Wei[1], and Jiun-Huei Proty Wu[3]
[1] Institute of Astronomy and Astrophysics, Academia Sinica, P.O. Box 23-141, Taipei 106, Taiwan
[2] Australia Telescope National Facility, Epping, NSW 1710, Australia
[3] National Taiwan University, Taipei 106, Taiwan
[4] Harvard-Smithsonian Center for Astrophysics, 60 Garden Street, Cambridge, MA 02138, USA
[5] Carnegie-Mellon University, Pittsburgh, PA 15213, USA
[6] Tamkang University, 251-37 Tamsui, Taipei County, Taiwan; ctli@asiaa.sinica.edu.tw
Received 2009 August 18; accepted 2010 January 6; published 2010 May 21

ABSTRACT

A wideband analog correlator has been constructed for the Yuan-Tseh Lee Array for Microwave Background Anisotropy. Lag correlators using analog multipliers provide large bandwidth and moderate frequency resolution. Broadband intermediate frequency distribution, back-end signal processing, and control are described. Operating conditions for optimum sensitivity and linearity are discussed. From observations, a large effective bandwidth of around 10 GHz has been shown to provide sufficient sensitivity for detecting cosmic microwave background variations.

Key words: cosmic background radiation – instrumentation: interferometers – telescopes

Online-only material: color figures

1. INTRODUCTION

Interferometric observations have gained much popularity in the study of the cosmic microwave background (CMB) anisotropy (White et al. 1999; Carlstrom et al. 2002; Padin et al. 2002; Leitch et al. 2002; Zwart et al. 2008), due to their advantage in stability and phase preserving characteristic via the heterodyne scheme for correlation and polarization observations. The cross-correlations used in an interferometric array can effectively suppress many systematics. To achieve high brightness sensitivity, broadband low noise receivers and matching correlators are the two most important components for a continuum interferometer. The advance in millimeter and microwave detector technologies in recent years has produced very broadband components. Low-noise amplifiers (LNAs) with bandwidths of 10 GHz or more are easily accessible with noise performance comparable to bolometric direct detectors, e.g., ACBAR (Runyan et al. 2003) with bandwidths of 30–40 GHz and an equivalent noise temperature or RJ temperature loading $T_{\rm RJ}$ between 40 K and 70 K. The CMB interferometers are therefore very competitive at millimeter wavelengths as compared to bolometers which are usually preferred at shorter wavelengths.

The Yuan-Tseh Lee Array for Microwave Background Anisotropy (AMiBA; Lo et al. 2001; Ho et al. 2009) is a radio interferometric array for the study of the CMB at 3 mm wavelength. AMiBA detects the minute deviations of the nearly constant CMB temperature over the sky and can study the spatial variation of this temperature fluctuation. In particular, AMiBA is imaging galaxy clusters via the Sunyaev–Zel'dovich effect (SZE; Sunyaev & Zel'dovich 1970, 1972; Birkinshaw 1999) for the first time at 3 mm wavelength. The array presently consists of 13 elements of 1.2 m reflectors distributed on a 6 m diameter platform. The receiver attached to each reflector is dual-polarization and equipped with cryogenically cooled LNAs operating in the 84–104 GHz frequency range. The intermediate frequency (IF) is from 2 to 18 GHz and is matched with a wideband analog correlator.

The strong interest in CMB observations has motivated the development of very broadband correlators with a limited spectral resolution. Utilizing a filter bank and complex correlators, Padin et al. (2002) built an analog correlator with 10 GHz bandwidth. Harris & Zmuidzinas (2001) worked on a different approach toward broadband operations by adopting an analog lag correlation scheme to build an auto correlator with a 4 GHz bandwidth. The AMiBA correlator is also based on the concept of the lag correlator and is designed to correlate the entire 16 GHz bandwidth. Recently, Holler et al. (2007) also reported a lag correlator for the Arcminute Microkelvin Imager with a 6 GHz bandwidth.

In principle, analog correlators can achieve better sensitivity over their digital counterparts due to the absence of the digitization process. Analog multipliers can easily achieve high sensitivity over multi-octave frequency ranges. In comparison the use of analog-to-digital converters (ADCs) is expensive and has limited bandwidth. Thus, the analog approach is preferred for observations which require high sensitivity but modest spectral resolution. However, the major difficulty in making a broadband system lies in the distribution and processing of the multi-octave signals coming from the antennas. Broadband impedance matching between components presents a major technical challenge for integrating a large-scale microwave system. Due to the nonlinear responses of an analog system, applying appropriate drive power levels and modulation/demodulation techniques to minimize the effects of the spurious terms are also very important. The AMiBA correlator is our attempt to address these technical issues. The four-lag analog correlator has a nominal 16 GHz bandwidth. This is currently the only correlator in operation with an effective correlation bandwidth of around 10 GHz.

The scientific goals and design philosophy of AMiBA are presented in Ho et al. (2009). A broader description of the

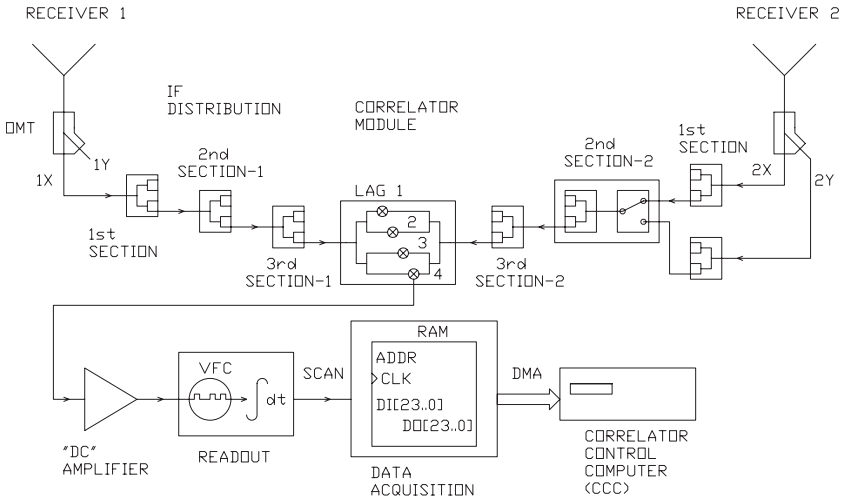

Figure 1. Block diagram of the AMiBA correlator. Signal flow for one baseline (1X2X) is presented. Following the correlator module, the signal flow for a particular lag (lag 4) is depicted.

AMiBA detection system is given in Chen et al. (2009), while a detailed description of the AMiBA hexapod mount can be found in Koch et al. (2009). From 2007 to 2008, observations were carried out with the seven-element array equipped with 60 cm dishes (Koch et al. 2006). Details on the observations and analysis of six massive galaxy clusters are presented in Wu et al. (2009). Subaru weak lensing data of four galaxy clusters were analyzed with the SZE data to derive the baryon fraction (Umetsu et al. 2009). This paper describes in detail the instrumental design and testing of the AMiBA correlator. We provide a system overview in Section 2 and major components of the system are described in Sections 3–7. In particular, we discuss various aspects of the correlator module in Section 4. In Section 8, we outline the testing and data processing. Finally, a conclusion on the system is given in Section 9.

2. SYSTEM OVERVIEW

As shown in Figure 1, the AMiBA correlator consists of five parts, namely the IF distribution, correlation, readout, data acquisition, and control. For the 13-element array, there would be a total of $(13 \times 12/2) \times 4 = 312$ correlations between the two polarizations of each receiver in order to obtain the four Stokes parameters for polarization measurements. In the AMiBA correlator, the number of correlator modules required is reduced by a factor of 2 by introducing two-way switches which choose between the two parallel-hand products, XX and YY, or the cross polarization products, XY and YX. For example, observations of the CMB spatial intensity variations require measurement of the XX and YY products only.

The network to distribute the 2–18 GHz IF from the receivers to the correlators is implemented by cascading three sections of four-way power dividers. The broadband analog lag correlator modules were designed using double-balanced diode mixers as the multipliers. The subsequent amplifier provides low-pass filtering with a 3 dB cutoff frequency at around 10 KHz.

In the readout electronics, we use voltage-to-frequency converters (VFCs) and counters to provide integrating analog to digital conversion of the multiplier outputs. This style of ADC has a slow response but a high dynamic range making them well suited to this application. The data acquisition electronics serve as a memory buffer between the readout electronics and the correlator control computer (CCC). In response to timed event signals from the CCC, it also generates control signals for phase switching, demodulation, and the readout process.

The CCC coordinates all the activities in the correlator, as well as archiving the data. Equipped with three special purpose cards from the Australia Telescope National Facility (ATNF), the CCC provides timing, data interface, and event signals for correlator operations. Further processing of the archived data is performed offline. This includes the processing required to transform the four lag domain measurements from each lag correlator into two complex channels in the frequency domain. In a digital lag correlator, the conversion from the lag domain to the frequency domain is a simple discrete Fourier transform. In the analog lag correlator, variations in gain and bandpass of the individual multipliers complicate the transform process considerably. Calibration with strong point sources such as planets becomes necessary. By observing a strong point source, the expected signal from each frequency bin of each baseline can be calculated. Correction to the transformation can then be extracted and applied to the following observations. A brief description of the relevant data processing and a demonstration are presented in Section 8.

3. IF DISTRIBUTION

An IF from 1 GHz to 21 GHz was proposed in the beginning of the project (Lo et al. 2001), but was subsequently changed to 2 GHz–18 GHz after taking into consideration the available commercial microwave components,[7] the complexity of the multi-octave circuit design, and the physical sizes of components. The IF signal distribution uses a mixture of off-the-shelf and specially designed microwave components.

After passing through the radio frequency (RF) LNAs and sub-harmonically pumped mixers (SHMs), which have a conversion loss of around 12 dB, the faint signals from the receiver inputs reach a level of −45 to −40 dBm. At this point, the noise figure of the subsequent components has a negligible contribution to the overall noise temperature, as long as the IF power level can be kept well above the thermal noise of about −71 dBm. Multiple broadband IF amplifiers are used along the IF chain to

[7] Commercial broadband microwave components usually come with a frequency range up to 18 GHz, or up to 26 GHz for the next available frequency range.

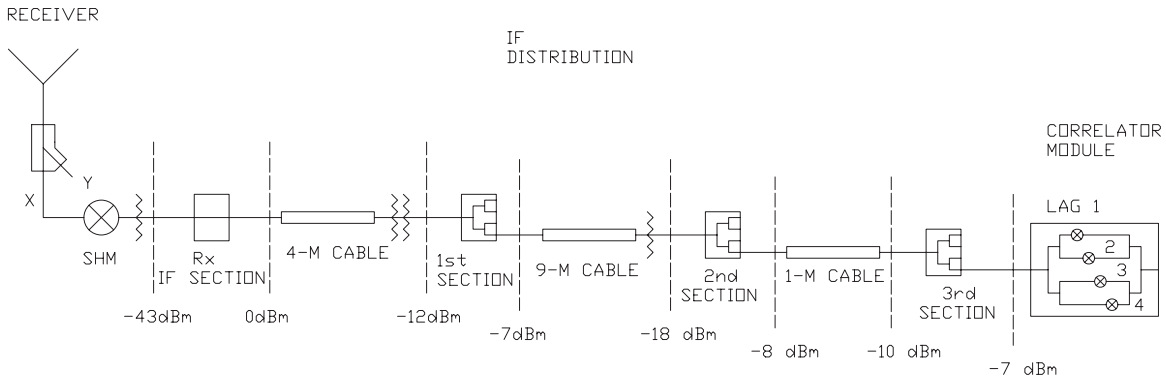

Figure 2. IF power profile from the receiver output to correlator module input (prior to 2009).

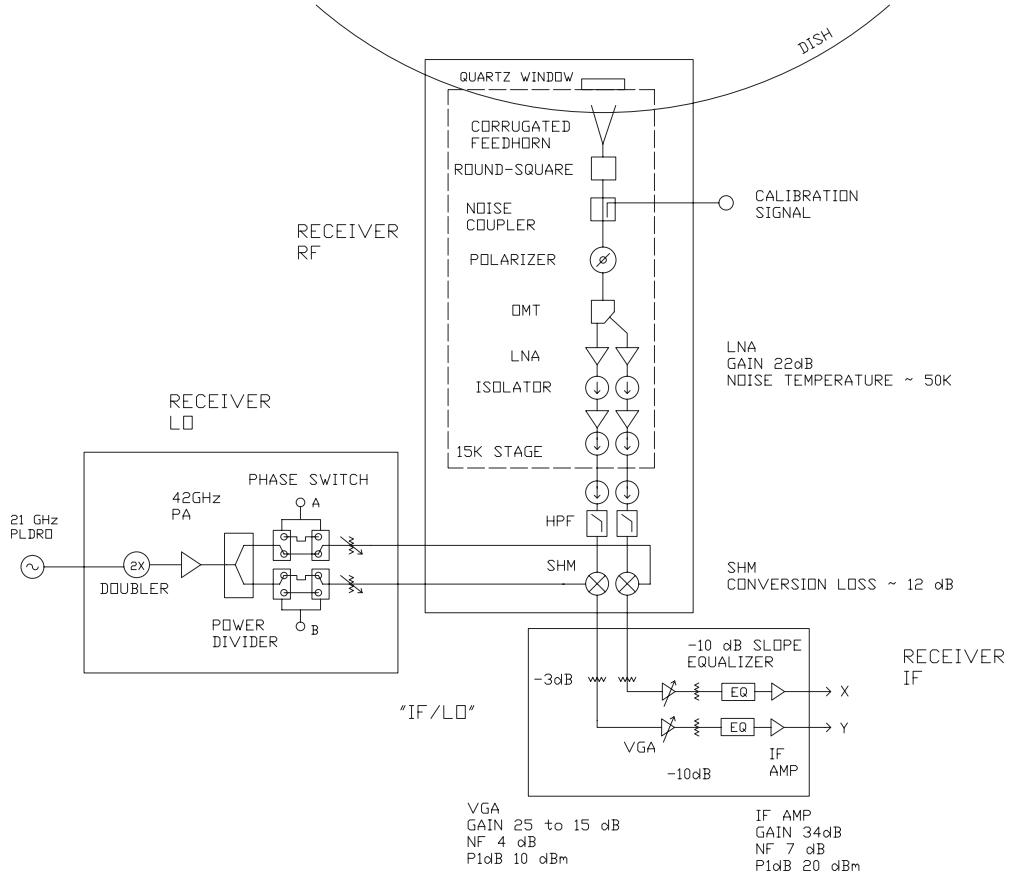

Figure 3. Schematic of the AMiBA receiver, including the RF, LO, and IF sections.

compensate for the divider loss. Attenuators are inserted along the IF paths to adjust the IF power level in order not to saturate the amplifiers and also to improve the matching between components. The input power level to the correlator modules is chosen to optimize the output signal-to-noise (S/N) ratio. The diagram of IF power level settings from receiver to correlator is shown in Figure 2.

Another issue is to keep the IF power stable over a period greater than the integration time of each data point. It was found that most of the gain variations can be attributed to ambient temperature changes (Nishioka et al. 2009). A ventilation system using fans and a feedback proportional-integral-derivative control was installed to minimize the temperature variations within the electronic cabinets (Jiang et al. 2009).

The following sections provide a description of each IF section. Schematics of the AMiBA receiver and correlator IF sections are shown in Figures 3 and 4, respectively, for reference.

3.1. First Section

In the first section, an IF amplifier[8] with a gain of 34 dB and output 1 dB compression point (P1dB) of 20 dBm is used in conjunction with a four-way power divider.[9] A directional coupler[10] sends part of the IF signal into a total power detector[11] to monitor the IF power after the receiver. The reading can be used to adjust the variable gain amplifier[12] (VGA) in the receiver

[8] CMA-18-2004, Teledyne Microwave.
[9] PDM-44M-10G, Merrimac.
[10] 1822, Krytar.
[11] 302A, Krytar.
[12] AVG4-02001800-40, Miteq.

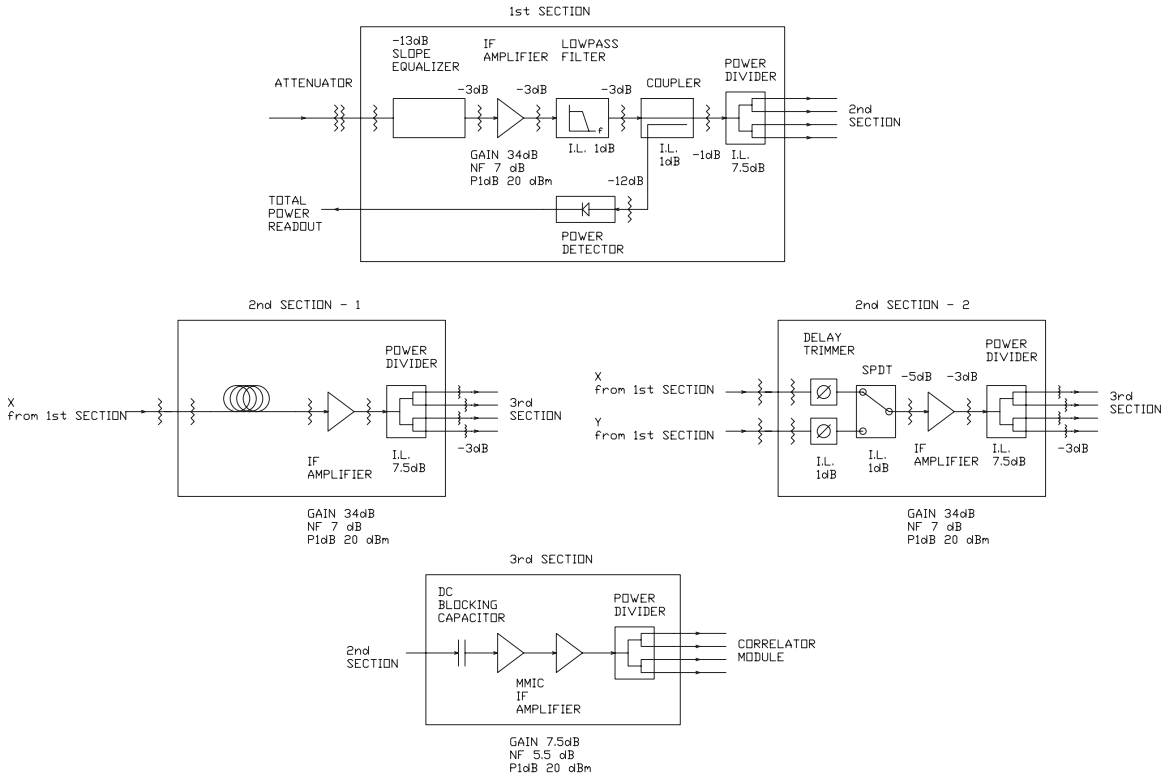

Figure 4. Schematic of the correlator IF sections. The gain, insertion loss (I.L.), noise figure (N.F.), and output 1 dB compression point (P1dB) of each component are listed where applicable.

IF to maintain the power level from the receiver. In addition to monitoring the receiver gain variations, the total power reading can also be used for sky dip or hot/cold load experiments to determine the sky and receiver noise temperature. The input of the total power readout electronics is switched between the signal and ground for alternating data. Common mode noise such as ground noise[13] is reduced after subtracting the ground reference from the signal.

An 18 GHz low-pass filter[14] determines the overall system bandwidth and also filters out the 21 GHz Local Oscillater (LO) leakage from the mixer. A 13 dB negative slope equalizer[15] compensates for the gain slope arising from the following components.

3.2. Second Section

There are two versions of the second section—one with a two-way switch,[16] a delay trimmer,[17] an IF amplifier, and a four-way power divider; the other with an IF amplifier, a power divider, and a delay compensation cable. During polarization observations, the two-way switches can be utilized to obtain four cross-correlations. The delay trimmer has a range of ±90 ps for fine delay tuning. The coarse delay adjustment is done by installing delay compensation cables of designated lengths. More details about delay trimming can be found in Lin et al. (2009).

[13] As the total power readout electronics input is connected to ground through a 1 MΩ resistor, the fluctuations on the reading can be seen. Similar effect can be observed as the readout is connected to the total power signal while the input of the 1st section is either terminated with a 50 Ω resistor or connected to a stable IF signal.

[14] 11SL10-1800/X24000-O/O, K&L Microwave.

[15] EQ1251-13M, Aeroflex/Inmet.

[16] 521-420803A, Dow-Key Microwave.

[17] 981, Aeroflex/Weinshel.

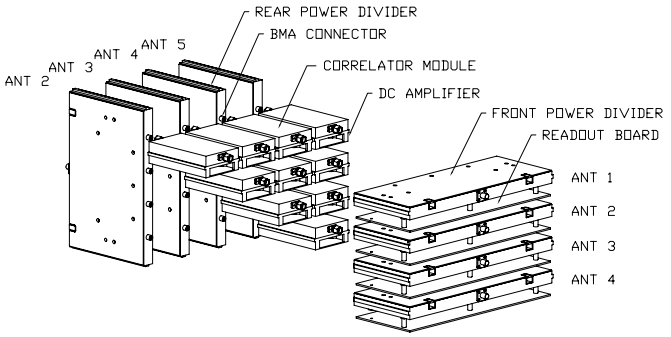

Figure 5. Modular layout of the correlator third section power dividers, correlator modules, DC amplifiers, and readout boards. The central portion consists of an array of lag correlators and DC amplifiers. The correlators are fed by power dividers at both ends. Readout boards underneath the horizontal power dividers are responsible for VFC ADC and integration.

3.3. Third Section

The third section consists of a four-way power divider with built-in amplifiers in front. Their dimensions are custom designed in order to feed the wideband IF signals into an array of correlator modules in a compact way as shown in Figure 5. The two stages of the MMIC IF amplifiers[18] with a cascaded gain of 14 dB are placed in front of the power divider to compensate for the loss in the power divider. A millimeter-wave DC-blocking capacitor[19] required for bias is placed in front of the first MMIC and rejects signals below 0.5 GHz. The power divider utilizes a Cu-clad substrate with an embedded resistive layer[20] which allows thin-film resistors to be etched into the circuit as part of

[18] TGA8300-SCC, Triquint Semiconductor.

[19] 500S100GT 50 XT, American Technical Ceramics.

[20] Arlon 25N + OhmegaPly.

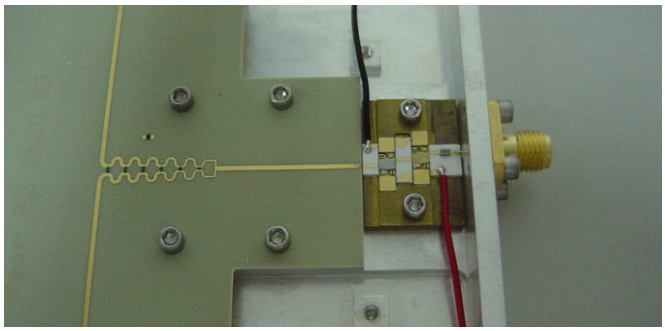

Figure 6. Picture of the MMIC IF amplifiers and power dividers used in the third section of the correlator IF. Bias circuit boards are not shown.
(A color version of this figure is available in the online journal.)

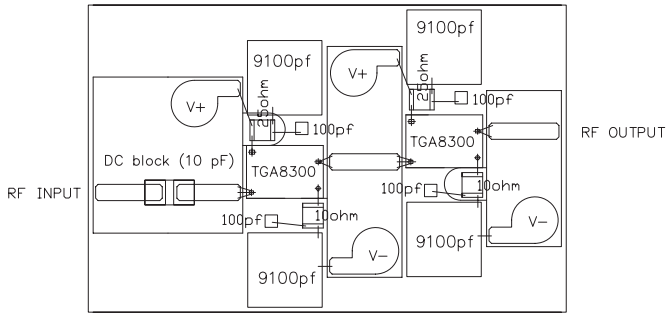

Figure 7. Assembly diagram for the IF amplifiers used in the third section of the correlator IF as recommended by the manufacturer, except the 100 pF bypass capacitors used to remove the oscillation at high frequencies.

the fabrication process. However, the same resistive layer causes significant loss and gain slope along a long transmission line. For cavity resonance suppression, metallic irises were extended down from the cover to confine the circuits into small channels. A picture of the custom power divider is shown in Figure 6. The component layout of the amplification stage and layouts of the two types of power dividers are also shown in Figures 7 and 8, respectively, for illustration. Details on the circuit design and test results can be found in Li et al. (2004).

4. CORRELATOR

4.1. Design and Specifications

In a lag correlator system as for AMiBA, a number of multipliers are used to measure the correlation as a function of the time offset or "lag" between two signals, namely,

$$r(\tau) = V_1(t) \star V_2(t) = \lim_{T\to\infty} \frac{1}{2T} \int_{-T}^{T} V_1(t) V_2^*(t-\tau) dt, \quad (1)$$

where τ is the lag between the two signals. The cross-correlation is represented by the pentagram symbol ($\star$) and V_2^* denotes the complex conjugate of V_2. The cross power spectrum of $V_1(t)$ and $V_2(t)$ can be derived via Fourier transforming the cross-correlation

$$V_1(t) \star V_2(t) \rightleftharpoons \hat{V}_1(\nu)\hat{V}_2^*(\nu). \quad (2)$$

In a lag correlator of the type described here, the correlation function is measured at discrete values of lags. The bandwidth of the correlator, BW, is determined by the delay increment $\delta\tau$ between measurements according to the Nyquist sampling theorem (Harris & Zmuidzinas 2001). The frequency resolution, δf, is determined by the number of lag measurements, N, such that $\delta f = \mathrm{BW}/(N/2)$.

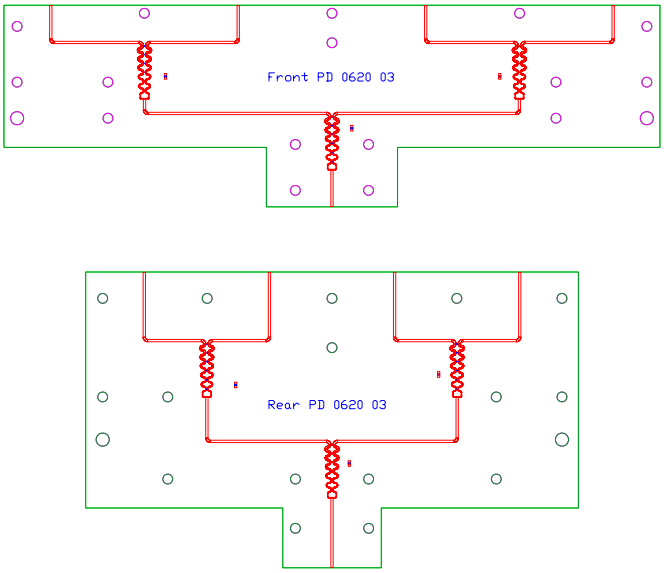

Figure 8. Layouts of the custom four-way power dividers.
(A color version of this figure is available in the online journal.)

To limit the gain loss from bandwidth smearing to an acceptable level, for an efficiency of $\sin(x)/x = 0.9$ at the primary beam half-power points, the fractional bandwidth must be at most

$$\frac{\delta\nu}{\nu} = \frac{1}{2}\frac{D}{B}, \quad (3)$$

where B is the baseline length and D is the dish diameter. Given the final configuration of the array (1.2 m dishes with longest baselines of about 6 m), a frequency resolution of 8 GHz is chosen. With a bandwidth of 16 GHz, the number of lags in the lag correlator is then set to four to provide two frequency channels. Correlator modules with more (e.g., eight) lags would not furnish much more information but would minimize the bandwidth smearing for the case of smaller diameter dishes. To examine the bandwidth smearing from another perspective, Figure 9 shows the calculated bandwidth patterns of the four lag outputs with an effective bandwidth of 16 GHz. The lag span is between ± 60 ps, enough to cover the delay for 1.2 m dishes with 6 m baselines.

For the AMiBA correlator, it is important to have a very wide bandwidth for CMB observations. To obtain the wide bandwidth, analog multipliers in the form of balanced mixers were employed. The use of passive multipliers circumvents the problem of $1/f$ noise and other noise from the bias circuitry usually associated with active multipliers. A flat amplitude response and a linear phase response (non-dispersive) are essential to achieve a large effective bandwidth. From tests with a translating noise source, the entire signal path with the four-lag correlator module has an effective bandwidth of around 10 GHz (Lin et al. 2009). A brief list of the AMiBA correlator specifications is given in Table 1.

Within each correlator module, two stages of two-way power dividers are cascaded to split the IF signals to feed four multipliers. The lags for each multiplier are specified to be 37.5, 12.5, -12.5, and -37.5 ps, respectively. The 25 ps lag spacing is designed to provide Nyquist sampling of the IF up to 20 GHz. The output voltages from the four lags are transformed into two complex data points in the cross power spectrum. The double-balanced mixers are comprised of low-barrier Silicon Schottky diode ring quads mounted between two wideband baluns. To

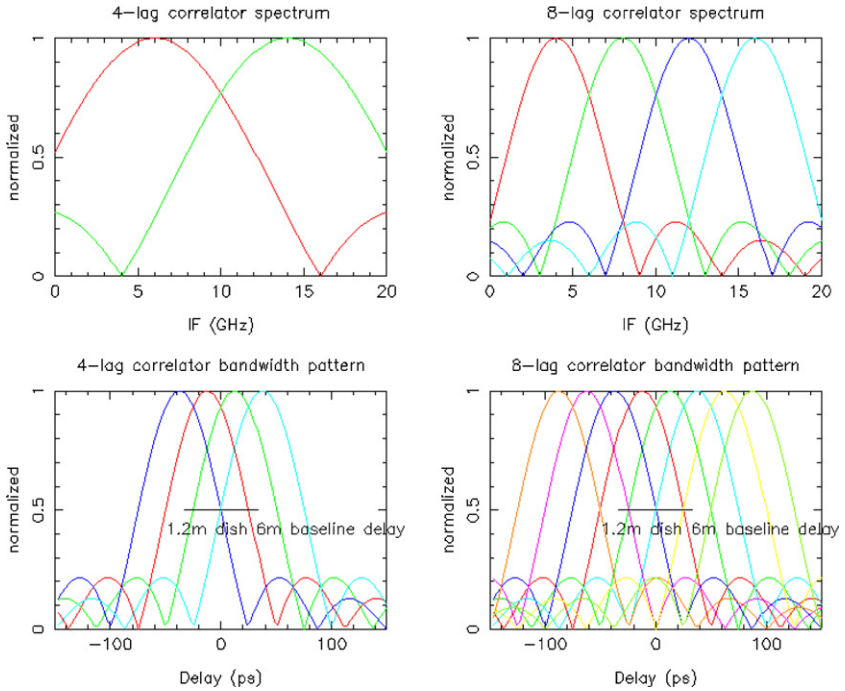

Figure 9. Upper left: recovered spectrum for a four-lag correlator with CW input signals at the center of two channels. Upper right: spectrum for an eight-lag correlator. Bottom left: bandwidth pattern for a four-lag correlator and delay range for 1.2 m dishes with 6 m baseline. Bottom right: bandwidth pattern for an eight-lag correlator. (A color version of this figure is available in the online journal.)

Table 1
AMiBA Four-lag Correlator Specifications

Characteristics	Specifications
Input frequency range	2–18 GHz
Responsivity	80 $V_{\rm rms}/W$ minimum
Responsivity variation vs. frequency	$< 3\ dB_{\rm pp}$
Phase response	$<$ 30 degree peak-to-peak deviation from linear
Delay increment accuracy	25.0 ± 2.5 ps
Input 1 dB compression point	>-5.0 dBm
Squared term contribution	<5%
Output impedance	<100 kΩ

avoid reflections due to discontinuities such as wire bonding between circuits, the entire circuit, including power dividers and baluns, is manufactured on a single microwave substrate. A picture of the four-lag correlator module manufactured by Marki Microwave Inc. is shown in Figure 10.

Regarding the channel isolation, for an ideal four-lag correlator, the recovered spectrum is $\Sigma_i\, c_i\, e^{-j\,\omega\,\tau_i}$, where c_i is the correlation measurement at each lag and τ_i is the nominal lag. If the input signals are continuous-wave (CW) signals at the center of each channel, namely 6 GHz and 14 GHz in our case, the recovered spectrum is shown in Figure 9 with a FWHM of about 12 GHz for each CW signal. Therefore, the leakage between channels is quite severe for the four-lag correlators. For comparison, the recovered spectrum of an ideal eight-lag correlator with input CW signals at the center of its four channels is also shown. Although the leakage between adjacent channels is still severe for an eight-lag module, the isolation between non-adjacent channels is acceptable. To improve on the channel isolation, one possibility is to apply a window function during the lag-to-visibility transformation. However, constrained by the small number of lags that we have, another possibility might be to apply bandpass filtering or a filter bank before correlation. The filter bank might also reduce the bandpass variation within each channel and maximize the effective bandwidth.

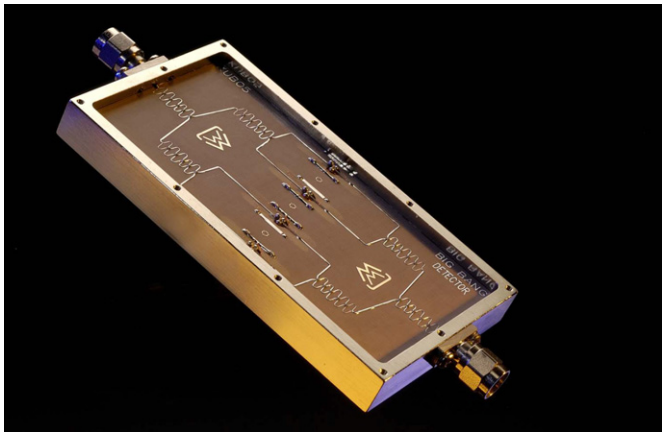

Figure 10. Four-lag correlator module manufactured by Marki Microwave Inc. The power dividers and multipliers can be seen.
(A color version of this figure is available in the online journal.)

4.2. Optimum Input Power

During observations, the correlator input signals consist of large uncorrelated noise signals from the receivers and tiny correlated signals from the sky. These large uncorrelated noise

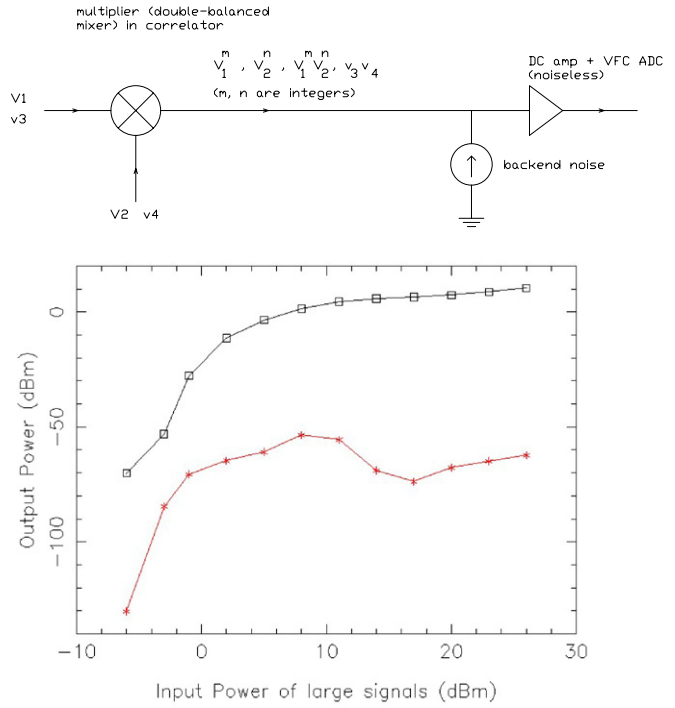

Figure 11. Upper: with v_1 and v_2 as the large uncorrelated noises, the output from a multiplier can be represented as the summation of various possible terms v_1^m, v_2^n, and $v_1^m v_2^n$, where m and n are integers. Each output term can contribute to correlator output fluctuations. On the other hand, v_3 and v_4 present the small correlated signals and $v_3 v_4$ is the expected product. A current noise source is used to represent the back-end noise from the DC amplifier and the VFC ADC at the input of the DC amplifier. Bottom: in the simulation of a double-balanced mixer with four tones, when the large signals have power below a certain level (−2 dBm), the product of two small signals (red curve) drops dramatically. As the input power of the large signals increases above the threshold, products of both small signals and large signals (black curve) increase linearly. As the input power keeps increasing (above 8 dBm), eventually both small-signal and large-signal products get compressed. Since a standard diode model is used during the simulations, the input power levels of the large signals where the diodes are sufficiently pumped or compressed are different from our measurements.

(A color version of this figure is available in the online journal.)

signals tend to pump the correlator diodes in much the same way as the local oscillator signal in a mixer application. This can lead to nonlinearity of the correlator multipliers and an excess of noise. We adjust the correlator input power level to reduce this degradation.

In a simulation of a double-balanced mixer with four tones (two with large power and two with 28 dB smaller power) as shown in Figure 11, when the large signals have a power below a certain level, the product of the two small signals drops dramatically. As the input power of the large signals increases above the threshold, the products of both small signals and large signals increase linearly, i.e., $p_{\rm out}$ proportional to $\sqrt{p_1 p_2}$. As the input power keeps increasing, eventually both small-signal and large-signal products become compressed. We can refer the large signals in the simulation to the uncorrelated noise from the receivers, and their product as the output fluctuations of the correlator, as the output fluctuation of the correlator is indeed due to the beating or mixing of uncorrelated signals (Kraus 1986). The small signals in the simulation are regarded as the correlated signals in the system. The simulation defines three regimes of operation, namely, underpumped, linear, and compressed. From experiments, our correlator modules have a linear range for input power from −20 dBm to −12 dBm, corresponding to output fluctuations with an rms from around 100 to 700 counts, including the back-end noise, as shown in Figure 12.

As the correlators are operated in the linear regime, it is seen that the correlator output fluctuations are proportional to $\sqrt{p_i p_j}$, where $p_{i,j}$ are the input power of each baseline (Wrobel & Walker 1999). Since there is no total power detector at the correlator module inputs, the input power cannot be measured directly, but can be inferred from the measured rms of each baseline. In the compressed regime, the output rms grows monotonically, although not linearly, as the input power increases. From the rms value, we can identify which of the three regimes (under-pumped, linear, and compressed) we are operating in. The gain can then be adjusted to optimize the S/N.

4.3. Spurious and Back End Noise

An ideal double-balanced mixer used as a multiplier can suppress even harmonics of both input signals and their products, i.e., v_1^n, v_2^m, and $v_1^n v_2^m$, where either n or m is even and $v_i (i = 1, 2)$ is the input voltage (Maas 1993). From simulations, it has been found that with a double-balanced mixer, the spurious terms such as v_1^2, v_2^2, and $v_1^2 v_2^2$ are suppressed by over 40 dB below the desired product $v_1 v_2$. Experiments show that residuals of these spurious terms can still be seen. They can be further suppressed by the use of a phase switching/demodulation process which allows the introduction of a DC blocking capacitor at the input of the low-frequency amplifier following the correlator module. Phase switching is achieved by switching a suitable delay into the LO path. However, as the LO signal is switched through different paths, a small amplitude modulation of the IF power level is introduced. This modulation survives the demodulation process and appears as an offset in the $v_1^2 v_2^2$ term. To minimize offset, variable attenuators are used to adjust the 42 GHz LO power to the SHM to minimize the IF power modulation.

S/N is optimized by operating the correlator in a slightly compressed regime, thereby ensuring that front-end noise dominates back-end noise from the DC amplifier and readout electronics. Figure 12 shows the output S/N estimated from the Jupiter fringes as the input power were varied. Most of the lag outputs show an increase in S/N as the input power (inferred from the output rms) increases, even when some of them were driven into the compressed regime.

A correlation interferometer where a multiplier is employed, the minimum detectable temperature or sensitivity is

$$\Delta T_{\rm min} = \frac{T_{\rm sys}}{\sqrt{2\Delta\nu\tau}}, \quad (4)$$

where $T_{\rm sys}$ is the system noise temperature, $\Delta\nu$ is the bandwidth, and τ is the integration time, assuming 100% efficiency (Kraus 1986). From the correlator output fluctuations, we can estimate the noise contributions from each part of the system, namely the front end (v_1^m, v_2^n, and $v_1^m v_2^n$ terms, where m and n are integers, v_1 and v_2 represent the large uncorrelated noises.) and back end (Figure 11), assuming all noises are uncorrelated, i.e., their variances are additive. Typical correlator output fluctuations measured under different conditions are listed in Table 2 to illustrate how the output noise might increase due to the spurious terms. As a result, noise contributions from the back end, as well as the spurious v_1^m, v_2^n terms can be estimated. Currently these spurious terms and the back-end noise reduce the S/N by 20%. An analysis of the system efficiency based on the observations with the seven-element array can be found in Lin et al. (2009).

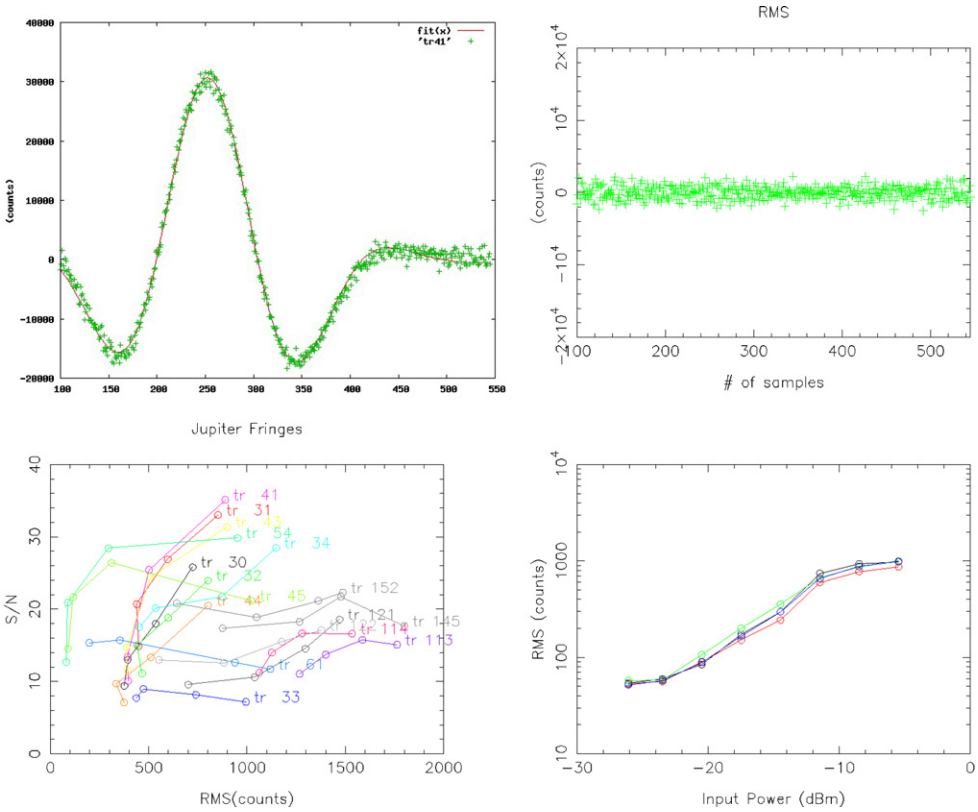

Figure 12. To determine the IF power for optimum S/N at correlator outputs, drift scans of Jupiter were taken with different input power levels to the correlator. The input power were varied by adjusting the VGAs along the IF paths. The input S/N was fixed and could be referred to the values at the receiver inputs. Output from the four-lag correlator module, usually referred to as the lag output, can be fitted to estimate the signal strength. During data processing, each of 168 lag outputs of the seven-element array is designated with a trace number. Upper left: one lag output (trace 41, labeled as tr41) is plotted (green crosses) and curve-fitted (red line) in terms of counts after the VFC ADC. Upper right: high-pass filtering is applied to the data to remove the low-frequency terms and the signal. The noise is estimated from the rms of the remaining fluctuations (green crosses). The responses of the lag correlators vary. Lower left: the S/N of several lag outputs (circles) is plotted against the rms values. Lines are drawn through data points of each output, and different colors are used for distinction. Lower right: for four lag outputs of one baseline, output fluctuations (rms in counts), including the back-end noise, are plotted (circles) as a function of the input power.

(A color version of this figure is available in the online journal.)

Table 2
Typical Results of the Correlator Output Fluctuations or rms Measured Under Four Conditions

Conditions	Measurements				Estimations	
	1	2	3	4		
Ant 2 (v_1)	Off	off	on	on		
Ant 3 (v_2)	Off	on	off	on		
YY lag 3 rms (counts)	95	783	805	1850	1120	1473
Noise composition	Back end	v_1^m terms, back end	v_2^n terms, back end	Overall	v_1^m terms, v_2^n terms, back end	$v_1^m v_2^n$ terms

Notes. When both receivers were off, the output noise could be attributed to the back-end noise from the DC amplifier and the ADC. When only one antenna was on, e.g., Ant 2, the output of the multiplier would include various terms from V_1. The situation was similar when only Ant 3 was on. For an ideal multiplier, the v_1^m and v_2^n terms are considered spurious. From the measurements, these terms also contributed to the output noise so that correlator output rms increased. Assuming that noise from each term can be summed in quadrature, we can estimate the output fluctuation when there is no v_1^m or v_2^n terms at the output and no back-end noise either, so as to determine how much the S/N has been degraded.

4.4. Low-frequency Amplifier

For the low-frequency LNA following the lag correlator module, because of the high output impedance of the mixers, low noise current amplifiers[21] were chosen to minimize the back-end noise. The bandwidth of the amplifier is limited in the feedback loop in order to reduce the output noise. Due to the phase switching, the correlated signals are square waves, at the phase switching frequency. A DC blocking capacitor is used in front of the amplifier to remove any DC term from the mixer output. As a result, the "DC" amplifier has a 3 dB passband from 0.1 to 9 kHz. The schematic of the DC amplifier is shown in Figure 13.

[21] OPA627AU.

5. READOUT ELECTRONICS

The correlator readout circuit uses a VFC plus a 24 bit counter as the ADC. The VFC generates pulse sequences at a frequency

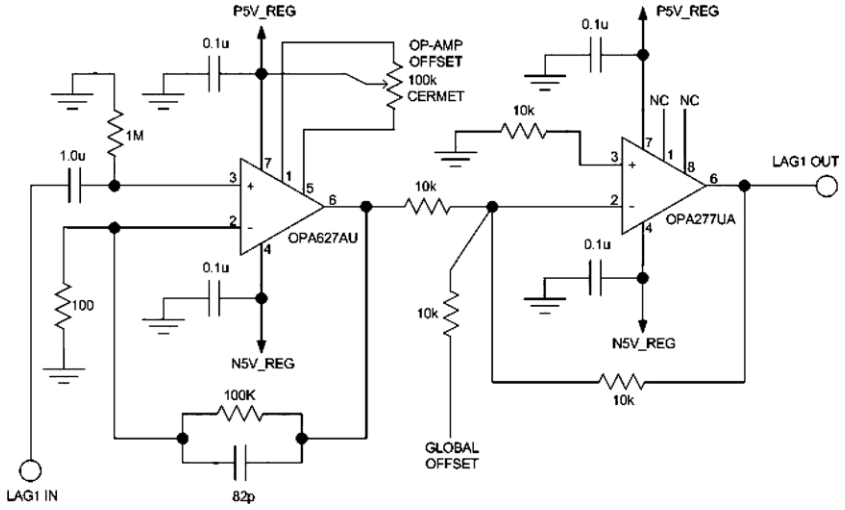

Figure 13. Schematic of the low-frequency or "DC" amplifier.

linearly proportional to the analog signal from the DC amplifier output. The up/down counter accumulates the pulses, acting as a long-term integrator as well as a phase switching demodulator. The up/down function is controlled by the demodulation signal.

In AMiBA correlator, there are four layers of processes used to remove systematics. The correlation process suppresses the uncorrelated receiver noise and gain fluctuations. The phase switching and demodulation process reduces the offsets or gain drifts that do not have the characteristics of the demodulation signals. One additional phase switching layer is implemented by inverting the sign of the demodulation signals for every other integration. Every two data points are then subtracted with respect to each other offline in the CCC. From analysis, the correlator output spectra show a white noise signature between 10^{-4} and 1 Hz, with an increase in power at lower frequency due to slow gain drifting (Nishioka et al. 2009). For the remaining offsets or false signals due to ground pick up, a two-patch scheme (Padin et al. 2002) is adopted. Observations are taken with, for our case, 3 minute tracking on the main field, and another 3 minute tracking on a trailing or leading field at the same declination, separated by a few minutes in right ascension. The main and the trailing/leading fields then share the same azimuth-elevation track with identical ground contamination of the data.

At the end of an integration interval, the contents of the counters are dumped into shift registers and serially scanned out by the data acquisition electronics. For the 13-element array, instead of the custom readout ICs used previously in the seven-element array (Li et al. 2004), discrete VFC components[22] are used. The digital section (counters/shift registers) is implemented in a field programmable gate array (FPGA). The new VFC is synchronous and has better linearity than the previous readout ICs. A schematic of the readout electronics with the timing diagram of the control signals is shown in Figure 14.

6. DATA ACQUISITION

The data acquisition circuit is used to store data from the readout circuits before they are transferred to the CCC via a direct memory access (DMA) process. Control signals, such as readout control signals and phase switching/demodulation signals are also generated here. RAM blocks configured as 128×24 bit RAMs within the FPGAs are allocated to store the correlation and total power data. There are two steps involved in transferring the data from the readout circuits to the CCC, scan, and DMA. Each step is triggered by events originating from the event generator (EG) in the CCC. The DMA process is ideal for transferring large volumes of data but is more efficient if the data are stored in consecutive addresses.

For the seven-element array, Walsh functions of 64 intervals per cycle are used as the phase switching signals. Currently there are five cycles in each integration of 0.226 s. This corresponds to a fastest switching frequency of around 700 Hz. For the 13-element array, Walsh functions of 128 intervals per cycle are used. Since the corner frequency of the $1/f$ noise from the passive diode multiplier we use is low, phase switching at rather low frequencies is feasible.

7. CONTROL

The operation of the AMiBA correlator is controlled by the CCC—an industrial grade PC running Linux. The CCC is equipped with three special cards—EG, Australia Telescope Distributed Clock (ATDC), and PCI Correlator Data Bus Interface (PCIIF) from ATNF.[23] The function of the EG is to generate events with precise timing. The PCIIF acts as an interface between the data acquisition circuit and the CCC to receive the DMA data. The interface appears as a 256 kbyte block of memory on the PCI bus while the PCIIF also assigns memory addresses and several control signals for the DMA process. Interrupts from the EG are relayed to the PCIIF for DMA timing. The ATDC provides precise timing for all the correlator operations and also generates an 8 MHz reference clock for digital processing in the data acquisition and readout circuits. The ATDC can phase-lock to both a 5 (or 10) MHz sine wave and a 1 pulse-per-second signal from a GPS receiver and is scheduled to synchronize the system clock of the CCC periodically. An alternative is to synchronize the system clock of the CCC to the GPS receiver via the network time protocol. A block diagram of correlator control components and signals is shown in Figure 15.

8. TESTING AND DATA PROCESSING

To test the response of each baseline, a *W*-band noise source is set up to translate between the two receiver inputs. The data of lag sequence can be Fourier transformed to obtain the bandpass

[22] AD7741, Analog Devices.

[23] http://www.atnf.csiro.au/technology/electronics/

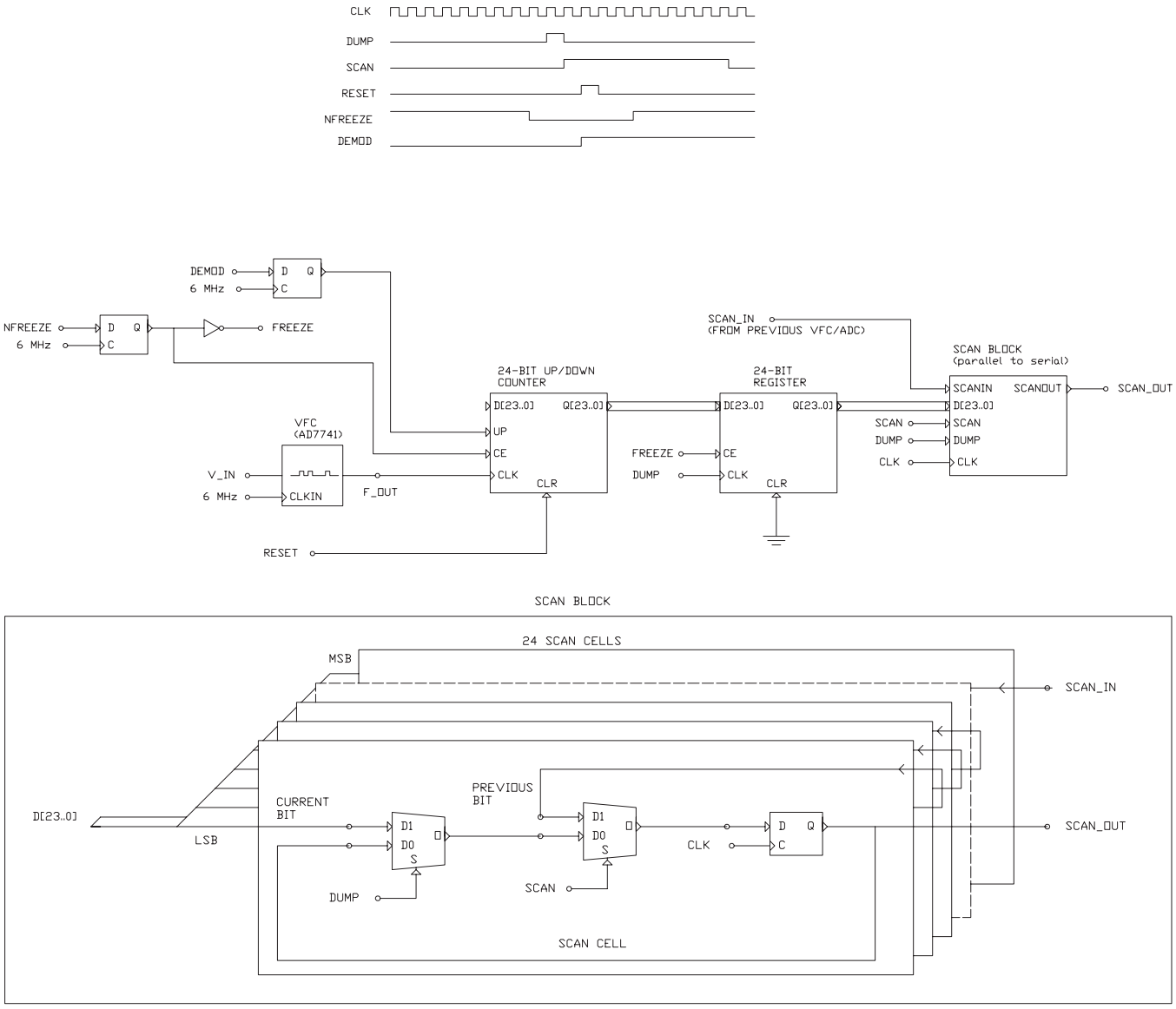

Figure 14. Upper: the timing diagram of the control signals and the schematic of the VFC/counter ADC used in the correlator for the 13-element array. Signals (dump, scan, reset, and demod—demodulation) are applied to the counter only when counting is stopped ("freezed"). "Freeze" needs to be buffered before being applied to the counter to avoid glitches. Since AD7741 is a synchronous VFC, i.e., the output pulse is initiated by the edge of the clock (CLKIN), "freeze" signal is buffered with a flip-flop triggered by the clock of the VFC. Bottom: schematic of the scan block used to transform 24 bit data into series of bits for the scan-out process.

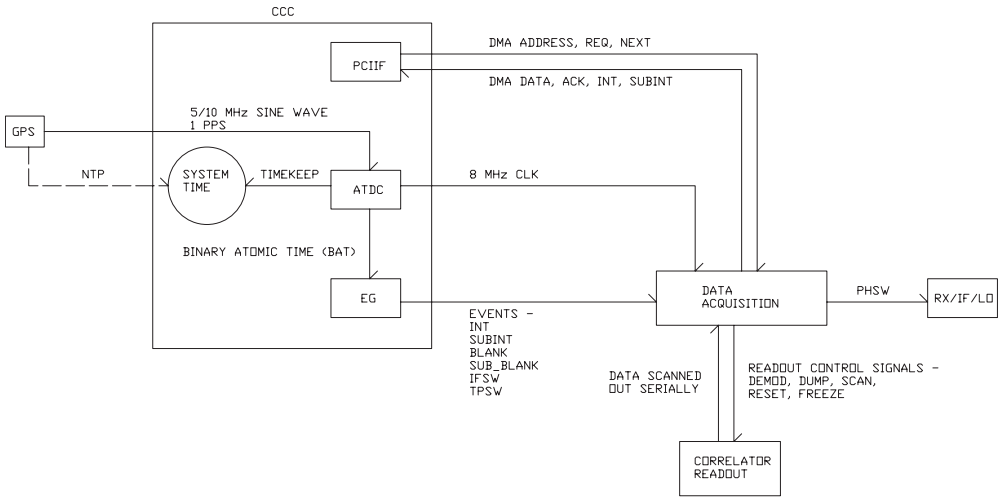

Figure 15. AMiBA correlator control block diagram.

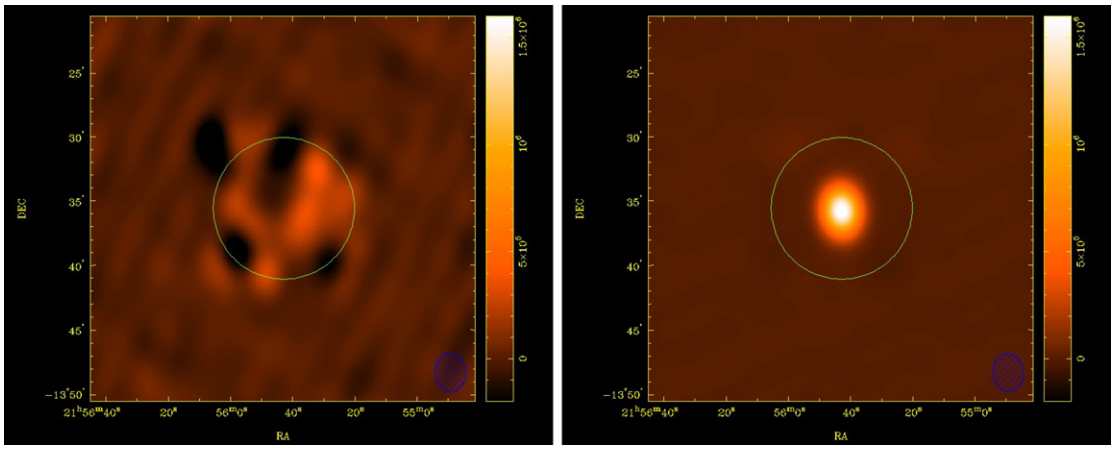

Figure 16. Cleaned images of Jupiter. Left: the image was formed with uncalibrated visibilities directly transformed from correlator outputs. Right: the constituent visibilities of the image have been calibrated by another set of Jupiter data. Both images are plotted with the same residual noise after CLEAN. The green circle indicates the FWHM of the primary beam, and the blue shaded ellipse at the bottom right corner represents the synthesized beam of the seven-element array in the compact configuration.

(A color version of this figure is available in the online journal.)

response. The bandpass shows a two-hump gain response and some scatter from a linear phase response. From the bandpass response, we can estimate the effective bandwidth B_e as

$$B_e = \frac{\left|\int W(f)\,df\right|^2}{\int |W(f)|^2\,df}, \tag{5}$$

where $W(f)$ is the complex bandpass response. The baselines of the seven-element array were estimated to have effective bandwidths ranging from 9 to 13 GHz (Lin et al. 2009).

With the derived bandpass responses, a transform matrix K can be created so that

$$[K][S] = [R], \tag{6}$$

where S is the complex column vector representing the input spectrum and R is the real column vector for the correlator output. K and S include both positive frequency terms and their complex conjugate at negative frequencies to yield real correlation products (Li et al. 2004).

With the correlation outputs from each baseline, we can invert K and then derive the spectra of the input signals or visibilities S via

$$[S] = [K]^{-1}[R]. \tag{7}$$

However, since the four lag outputs only give us two independent complex data points in the frequency spectrum, K is rather singular due to degeneracy. The singular value decomposition method can be used to invert K. Once K^{-1} is obtained, the spectra of n ($n > 2$) channels can be obtained. Eventually, we have to consolidate those n channels into two bands. Another approach would be to integrate the complex response matrix K in frequency into two bands first. The integrated matrix $\bar{K}$ can be easily inverted, and the two-band visibility output can be written as $[\bar{S}] = [\bar{K}]^{-1}[R]$.

From simulations, Lin et al. (2009) showed that given an accurate and high spectral resolution measurement of K, the visibility can be recovered regardless of the source offset from the phase center. On the other hand, inaccurate estimate of K results in errors in the recovered visibility. The error varies with the source offset and can be calibrated at any given offset by observing a point source at the same offset from the phase center. The calibration is strictly valid only in a small region (a small fraction of the synthesized beam) around the location at which the calibration source is observed. At other locations within the field of view, there are gain and phase errors set by uncertainties in the lag-to-visibility transformation that affect the quality of the image reconstruction, although further calibration should reduce these errors. However, further simulations show that applying the calibration to the entire field of view only contributes about 2% in rms to the recovered point source flux after combining data from all baselines (Lin et al. 2008).

Although using a translating noise source at the receiver inputs to create artificial fringes is a useful method to measure the transfer function of the correlator, it is hard to run the test inline with observations. The spectral resolution obtained with our current setup was not sufficient. This approach becomes more tedious as the number of baselines increases and we would still need to use the planet data to calibrate the gain and phase of each baseline. An alternative would be to derive the response matrix K in two bands, assuming nominal responses of an ideal lag correlator. Data from tracking of strong point sources such as Jupiter, Saturn, or Mars, performed regularly at an interval of approximately 3 hr during the observations, can be used for calibration. All data analysis and calibrations were restricted to observations made at the phase center at the moment. Figure 16 shows the images of Jupiter from visibilities with and without calibration. The calibrator was another set of data of Jupiter taken several minutes apart. The uncalibrated visibilities suffer from errors in the transformation as mentioned above. Forming an image directly results in very strong cancellation. After calibration, the visibilities add up coherently and form a strong point source at the phase center. The images have been deconvolved using the CLEAN algorithm (Hogbom 1974) and plotted with the same dynamical range. More details about data processing can be found in Wu et al. (2009) and Lin et al. (2009).

9. CONCLUSION

From observations, the AMiBA correlator has proven to have the sensitivity required for CMB detection. The analog multipliers used in the lag correlators provide the wide bandwidth required for high sensitivity. The inherent noise rejection of the interferometer is also very beneficial. Compared with the filter bank scheme used by CBI (Padin et al. 2002), the lag correlator design is simpler and more compact. Large bandwidth

with a small number of lags does not present a significant challenge for the lag-to-visibility transformation after proper calibrations. At the moment, the effective bandwidth we can achieve is limited by bandpass variations due to wideband impedance matching. However, a significant portion (60%) of the nominal bandwidth has been achieved. To improve on the bandpass variations, it is possible to operate the correlator at a higher IF, since the response of the analog multipliers is not limited to frequencies of few GHz. Thus, with a similar fractional bandwidth, a larger bandwidth could be achieved. Wideband complex correlators in conjunction with bandpass filters can also be considered. For AMiBA, complex correlators with a bandwidth of 8 GHz are suitable. By interleaving a number of them in frequency, a large bandwidth is feasible. The filters would also improve the isolation between channels. Similar analog interferometric systems can be constructed for high sensitivity, high angular resolution, and moderate frequency resolution observations.

We thank the administrative staff for their support over the years. We thank A. Harris for useful discussions and notes. We thank the Ministry of Education, the National Science Council, and the Academia Sinica for their support of this project. We thank the NOAA for accommodating the AMiBA project on their site on Mauna Loa. We thank the Hawaiian people for allowing astronomers to work on their mountains in order to study the universe. This work is partially supported by the National Science Council of Taiwan under the grant NSC98-2119-M-001-024-MY4.

REFERENCES

Birkinshaw, M. 1999, Phys. Rep., 310, 97
Carlstrom, J. E., et al. 2002, ARA&A, 40, 643
Chen, M.-T., et al. 2009, ApJ, 694, 1664
Harris, A. I., & Zmuidzinas, J. 2001, Rev. Sci. Instrum., 77, 1531
Ho, P. T. P., et al. 2009, ApJ, 694, 1610
Hogbom, J. A. 1974, A&AS, 15, 147
Holler, C. M., et al. 2007, A&A, 464, 795
Jiang, H., et al. 2009, I2MTC 2009 (Los Alamitos, CA: IEEE), 1268
Koch, P., et al. 2006, in Proc. EuCAP 2006, ed. H. Lacoste & L. Ouwehand (ESA SP-626; Noordwijk : ESA), 668.1
Koch, P., et al. 2009, ApJ, 694, 1670
Kraus, J. D. 1986, Radio Astronomy (2nd ed.; Durham, N. H.: Cygnus-Quasar)
Leitch, E. M., et al. 2002, ApJ, 568, L28
Li, C.-T., et al. 2004, Proc. SPIE, 5498, 455
Lin, K.-Y., et al. 2008, Proc. SPIE, 7012, 701207
Lin, K.-Y., et al. 2009, ApJ, 694, 1629
Lo, K. Y., et al. 2001, in AIP Conf. Proc. 586, Relativistic Astrophysics, 20th Texas Symp., ed. J. C. Wheeler & H. Martel (Melville, NY: AIP), 172
Maas, S. A. 1993, Microwave Mixers (2nd ed.; Norwood, MA: Artech House)
Nishioka, H., et al. 2009, ApJ, 694, 1637
Padin, S., et al. 2002, PASP, 114, 83
Runyan, M. C., et al. 2003, ApJS, 149, 265
Sunyaev, R. A., & Zel'dovich, Y. B. 1970, Comments Astrophys. Space Phys., 2, 66
Sunyaev, R. A., & Zel'dovich, Y. B. 1972, Comments Astrophys. Space Phys., 4, 173
Umetsu, K., et al. 2009, ApJ, 649, 1643
White, M., et al. 1999, ApJ, 514, 12
Wrobel, J. M., & Walker, R. C. 1999, in ASP Conf. Ser. 180, Synthesis Imaging in Radio Astronomy II, ed. G. B. Taylor, C. L. Carilli, & R. A. Perley (San Francisco, CA: ASP), 171
Wu, J.-H. P., et al. 2009, ApJ, 694, 1619
Zwart, J. T. L., et al. 2008, MNRAS, 391, 1545